Nanoscale

PAPER

View Article Online
View Journal | View Issue

Cite this: *Nanoscale*, 2024, **16**, 13895

# Conductivity-mediated *in situ* electrochemical reconstruction of $CuO_x$ for nitrate reduction to ammonia†

Hao Liang,‡[a] Yinqiao Zhang,‡[a] Xiaona Zhang,[a] Erzhuo Zhao,[c] Wendan Xue,[d] Enguang Nie,[e] Jianqiu Chen,*[a] Sijin Zuo*[a] and Minghua Zhou[b]

The electrocatalytic nitrate reduction reaction ($NO_3RR$) is an ideal $NH_3$ synthesis route with ease of operation, high energy efficiency, and low environmental detriment. Electrocatalytic cathodes play a dominant role in the $NO_3RR$. Herein, we constructed a carbon fiber paper-supported $CuO_x$ nanoarray catalyst (CP/$CuO_x$) by an *in situ* electrochemical reconstruction method for $NO_3^-$-to-$NH_3$ conversion. A series of characterization techniques, such as X-ray diffraction (XRD) and *in situ* Raman spectroscopy, unveil that CP/$CuO_x$ is a polycrystalline-faceted composite copper nanocatalyst with a valence composition containing $Cu^0$, $Cu^+$ and $Cu^{2+}$. CP/$CuO_x$ shows more efficient $NO_3^-$-to-$NH_3$ conversion than CP/Cu and CP/$Cu_2O$, which indicates that the coexistence of various Cu valence states could play a dominant role. CP/$CuO_x$ with a suitable $Cu^{2+}$ content obtained by adjusting the conductivity during the *in situ* electrochemical reconstruction process exhibited more than 90% faradaic efficiencies for the $NO_3RR$ in a broad range of −0.3 to −1.0 V *vs.* RHE, 28.65 mg $cm^{-2}$ $h^{-1}$ peak ammonia yield, and stable $NO_3RR$ efficiencies for ten cycles. These findings suggest that CP/$CuO_x$ with suitable copper valence states obtained by fine-tuning the conductivity of the electrochemical reconstruction may provide a competitive cathode catalyst for achieving excellent activity and selectivity of $NO_3^-$-to-$NH_3$ conversion.

Received 13th April 2024,
Accepted 4th June 2024

DOI: 10.1039/d4nr01625d

rsc.li/nanoscale

## 1. Introduction

Ammonia ($NH_3$), as the essential chemical feedstock of pharmaceutical manufacturing, fertilizer production, energy supply, *etc.*, plays an important role in global energy and agricultural production.[1,2] At present, industrial-scale $NH_3$ synthesis is dominated by the energy-intensive Haber–Bosch (H–B) process. However, the H–B process requires high temperature (400–500 °C) and high pressure (150–300 atm), leading to the consumption of 2% of the world's annual energy output and 400 Mt of carbon dioxide emission per year.[3] Therefore, finding a new method for $NH_3$ synthesis that is environmentally friendly, efficient, and can utilize renewable energy sources has important research value and application prospects.

Electrocatalytic technologies are beginning to show their potential in $NH_3$ synthesis due to their ease of operation, high energy efficiency, and low environmental detriment.[4–6] The electrocatalytic nitrate reduction reaction ($NO_3RR$) is an ideal $NH_3$ synthesis route, which not only complements the traditional energy-intensive and costly $NH_3$ production process, but also helps to alleviate the environmental problems caused by nitrate pollution (such as eutrophication).[7–10] Nitrate reduced to ammonia would undergo a multi-step electroreduction process at the cathode that involves the transfer of nine protons and eight electrons to ultimately produce $NH_3$ and $H_2O$ in acidic and neutral electrolytes.[11,12] Throughout the electrochemical reaction at the cathode, the rate-determining step (*$NH_3$ to $NH_3$) and the competing hydrogen evolution reaction (HER) dominantly impede the kinetics and faradaic efficiency of the $NO_3RR$.[13–16] As a result, it is crucial to rationally design cathode catalysts to achieve excellent activity and selectivity of the $NO_3RR$.

Various catalysts, including noble and transition metals, alloys, and non-metallic electrodes, have been explored to

---

[a] *State of Key Laboratory of Natural Medicines, School of Engineering, China Pharmaceutical University, Nanjing 210009, PR China. E-mail: sjzuo@cpu.edu.cn, cjqer@163.com*

[b] *Key Laboratory of Pollution Process and Environmental Criteria, Ministry of Education, College of Environmental Science and Engineering, Nankai University, Tianjin 300350, PR China*

[c] *School of Environment, Tsinghua University, Beijing 100084, PR China*

[d] *Department of Chemistry, Tsinghua University, Beijing 100084, PR China*

[e] *College of Bioscience and Biotechnology, Yangzhou University, Yangzhou, 225009, PR China*

† Electronic supplementary information (ESI) available. See DOI: **https://doi.org/10.1039/d4nr01625d**

‡ These authors contributed equally to this work.

enhance the selectivity and efficiency of the $NO_3RR$.[17,18] For example, Liu *et al.* developed atomically precise silver (Ag) nanocluster catalysts for an efficient $NO_3RR$ to synthesize $NH_3$, achieving high stability in neutral media.[19] A transition metal-based Ni/$Ni(OH)_2$ catalyst was reported to enable ammonia production at ampere-level current densities. Metal-free amorphous graphene was also found to benefit the direct electroreduction of nitrates to ammonia.[20] However, common issues with these catalysts include their limited availability, high cost, and potential deactivation over long-term use. Copper (Cu), on the other hand, shows promise in addressing these issues due to its abundance, lower cost, and superior $NO_3^-$ adsorption and reduction of $*NO_3$ to $*NO_2$, which is attributed to the highly occupied d-orbitals and the energy level of Cu matching the lowest unoccupied $*\pi$ orbital of $NO_3$-N.[21] Nevertheless, pure Cu would rapidly deactivate owing to the $NO_3RR$ intermediates (*e.g.*, $NO_2^-$) accumulating on the Cu surface.[22] To overcome this limitation, researchers have proved that optimizing the valence state of Cu is a preferable way, as $Cu^{\delta+}$ species (*e.g.*, $CuO_x$) with a relatively low energy barrier for the $NO_3RR$ are more active in adsorbing, activating, and even desorbing the intermediates.[23–25] For instance, Wu *et al.* reported a strategy for controlling the oxidation state of copper using aryl diazonium salts for covalently binding aryl groups onto the copper surface.[26]

In this study, a carbon fiber paper-supported $CuO_x$ nanoarray catalyst (CP/$CuO_x$) obtained by an *in situ* electrochemical reconstruction method was used for $NO_3^-$-to-$NH_3$ conversion. The crystalline state, morphology, and electronic state of Cu were investigated by various spectroscopy characterization techniques. The performance of the CP/$CuO_x$ cathode was assessed in the electrocatalytic reduction of $NO_3^-$ to $NH_3$ including $NH_3$ yield, faradaic efficiency and stability. The electrochemical measurements, density functional theory (DFT) calculations, and spectroscopy characterization studies of CP/Cu, CP/$Cu_2O$ and CP/$CuO_x$ cathodes were compared to evaluate the role of $CuO_x$ in $NO_3^-$-to-$NH_3$ conversion. Finally, the effects of different physicochemical morphologies of CP/$CuO_x$ constructed by conductivity modulation on $NH_3$ yield and faradaic efficiency were investigated.

## 2. Materials and methods

### 2.1 Working electrode preparation

The CP/Cu precursor was first synthesized using a chronoamperometry (*i*–*t*) method. As shown in Scheme 1, a carbon fiber paper sheet was used as the cathode (1 cm × 2 cm), a platinum sheet was used as the anode, and a saturated calomel electrode (SCE) was used as the reference electrode, respectively. 25 mL of electrolyte containing 70 mM $CuSO_4$ and 0.50 M $Na_2SO_4$ solution was added to a single-cell reactor. Then copper ions can be electrochemically reduced to metallic copper and deposited onto the carbon fiber paper at a constant stirring rate of 600 rpm and a deposition potential of 0.3 V *vs.* RHE for a duration of 800 seconds.

The acquired CP/Cu precursor was immersed in an alkaline solution which consisted of 2.5 M NaOH and 0.125 M $(NH_4)_2S_2O_8$ for 15 min to convert Cu to $Cu(OH)_2$. After washing 3–5 times with deionized water, the $Cu(OH)_2$ was dried. The $Cu(OH)_2$ was then pyrolyzed to obtain $Cu_2O$-loaded CP (CP/$Cu_2O$) at 550 °C for 2 hours in a tube furnace (inert gas atmosphere).

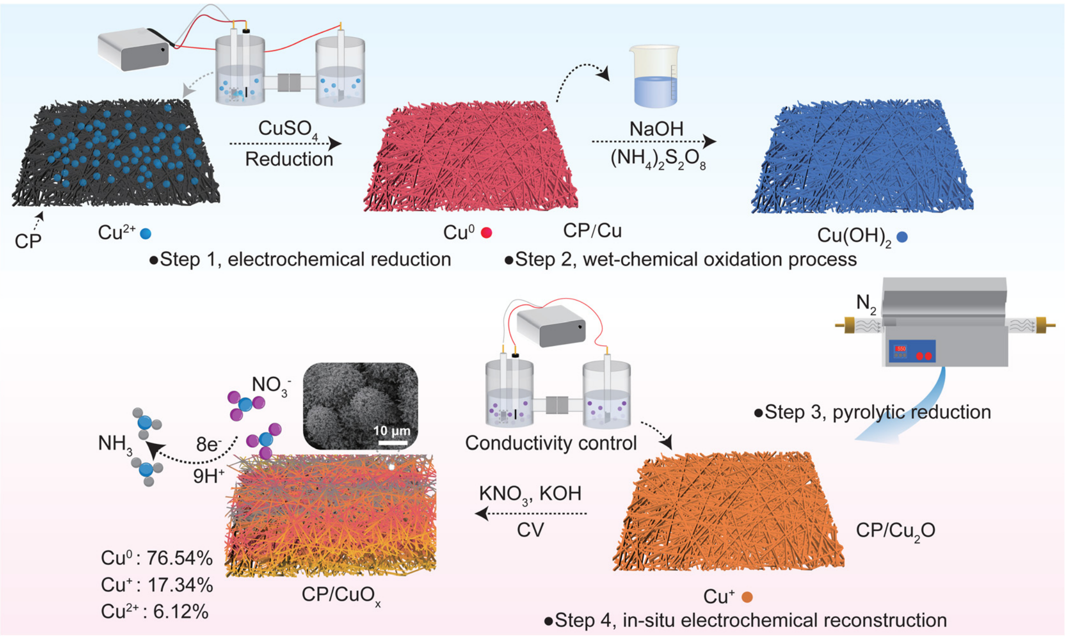

**Scheme 1** Schematic illustration of the synthesis of CP/$CuO_x$.

CP/$Cu_2O$ was treated by cyclic voltammetry (CV) for 50 electrolysis cycles (−0.5 to 0.2 V *vs.* RHE) in the alkaline electrolyte (1 M KOH) with varying nitrate concentrations, as displayed in Scheme 1. The nitrate concentrations of the alkaline electrolyte used were 0.1, 0.5, 0.8, and 1 M, and the corresponding conductivities of the electrolytes were 112, 128, 138, and 143 μS $cm^{-1}$, respectively.

### 2.2 Ammonia electrosynthesis

Electrochemical measurements were performed in an H-cell configured with the anodic and cathodic chambers (100 mL each) being separated by an anion exchange membrane (Nafion 115). 60 mL of 1 M KOH containing 0.1 M $KNO_3$ was added to each chamber. CP/$CuO_x$ was used as the working electrode. Electrochemical methods including CV, linear scanning voltammetry (LSV), and electrochemical impedance spectroscopy (EIS) were used for characterization of the $NO_3$RR performance of the CP/$CuO_x$ catalysts. LSV tests were performed in the range of −1 to 1 V *vs.* RHE at 5 mV $s^{-1}$. CV curves were recorded in the range of −0.52 to −0.62 V *vs.* RHE at 20, 40, 60, 80, 100, and 120 mV $s^{-1}$ in 1 M KOH. EIS was conducted at 0.15 V *vs.* RHE and frequencies from 0.1 to 100 kHz. The measurement methods of $NO_2^-$, $NO_3^-$, $NH_4^+$, $N_2H_4$, $N_2$ and $H_2$ are depicted in the ESI,† and their standard curves are shown in ESI Fig. S1–S5.†

## 3. Results and discussion

### 3.1 Preparation and characterization of electrodes

The preparation process of the CP/$CuO_x$ electrode is shown in Scheme 1. First, the CP was pre-treated to remove the impurities on the fiber surface and to improve the attachment point of the copper grains. CP loaded with copper grains (CP/Cu) was obtained by chronoamperometry, and the optimum copper deposition state was obtained by tuning the deposition potential and reaction time (ESI Fig. S6 and S7†). The copper grains on CP/Cu were converted to $Cu(OH)_2$ by wet chemistry. They were then annealed to obtain CP/$Cu_2O$ by the thermal decomposition method. Finally, CP/$Cu_2O$ was reduced to a composite Cu nanocatalyst (CP/$CuO_x$) with better electrochemical stability in solutions containing nitrates. During the *in situ* electrochemical reconstruction process, the CV curves of the first 40 cycles varied significantly and with little overlap, indicating that $Cu_2O$ was reduced on the surface of the carbon fibers (ESI Fig. S8a and b†). In subsequent cycles, the CV curves show good overlap, demonstrating that the catalyst has formed a stable chemical state (ESI Fig. S8c and d†).

As shown in Fig. 1a and b, after the *in situ* electrochemical reconstruction process, CP/$CuO_x$ formed a cluster-like structure consisting of many spherical nanograins on its surface at a conductivity of 112 μS $cm^{-1}$. The characteristic diffraction peaks of C, Cu and $Cu_2O$ are observed in the XRD spectra of the CP/$CuO_x$ electrocatalyst, as shown in Fig. 1c and ESI Table S1.† The diffraction peaks of C are from the graphitic carbon structure of the CP, with 26.5° being attributed to the (002) facet and 54.5° being attributed to the (004) plane of the carbon substrate.[27] The weaker diffraction peaks observed at 43.3° and 50.5° are attributed to the Cu (100) facet and the Cu (111) plane, respectively. It is important to note that the (200) diffraction peak is a secondary diffraction originating from the (100) plane.[28,29] The CP/$CuO_x$ electrocatalyst showed weakly (100)- and (111)-oriented CuO crystalline phases and also strongly (100)-, (111)-, and (220)-oriented $Cu_2O$ crystalline phases. The elemental composition and valence states of CP/$CuO_x$ were further investigated by XPS. One can see in Fig. 1d that CP/$CuO_x$ exhibits the characteristic peaks of C 1s, O 1s, Cu LMM, Cu 2p3/2 and Cu 2p1/2.[30,31] As displayed in Fig. 1e, there are three different types of oxygens present in CP/$CuO_x$, namely $O_I$ (oxygen on the complex structure), $O_{II}$ (oxygen on the Cu/$Cu_2O$ structure) and $O_{III}$ (oxygen-deficient species).[32–35] This also indicates that CP/$CuO_x$ is a mixed-valence copper nanocatalyst. Fig. 1f shows the high-resolution Cu LMM XPS spectrum of CP/$CuO_x$. The three peaks observed at 567.76, 573.94 and 571.80 eV correspond to $Cu^0$ (76.54%), $Cu^+$ (17.34%) and $Cu^{2+}$ (6.12%), respectively.[36–38] In addition, our Cu 2p XPS spectrum (ESI Fig. S9†) also showed a similar phenomenon of mixed $Cu^{2+}$ and $Cu^+$/$Cu^0$. These results collectively demonstrated that CP/$CuO_x$ is a polycrystalline-faceted composite copper nanocatalyst.

### 3.2 Evaluation of ammonia electrosynthesis

The catalytic activity of CP/Cu, CP/$Cu_2O$ and CP/$CuO_x$ for the electroreduction of nitrate to ammonia was investigated in H-cells. Before investigating the $NO_3$RR performance of the catalysts, their LSV curves were tested until the polarization curves reached a steady state. Fig. 2a shows the LSV curves of the three catalyst. In general, the presence of $NO_3^-$ leads to an increase of current density for the three catalysts. The phenomenon indicates that the $NO_3^-$ reduction process occurred on the three catalysts.[39,40] Moreover, the current density of CP/$CuO_x$ with $NO_3^-$ shows the most significant increase compared to that of virgin CP, CP/Cu and CP/$Cu_2O$ (Fig. 2a and ESI Fig. S10†). In particular, at −0.4 V *vs.* RHE, the current density of CP/$CuO_x$ increased to −311 mA $cm^{-2}$, which is approximately 2.78 times higher than that of CP/Cu. The results suggest that more $NO_3^-$ reduction occurred on the CP/$CuO_x$ cathode.

In addition, we further investigated the kinetics of the $NO_3$RR by analyzing the Tafel curves of the three catalysts (Fig. 2b). CP/$CuO_x$ exhibited the smallest Tafel slope (194.09 mV $dec^{-1}$) compared to CP/Cu (255.06 mV $dec^{-1}$) and CP/$Cu_2O$ (233.55 mV $dec^{-1}$), suggesting that the composite state Cu interface of CP/$CuO_x$ is beneficial for improving the reaction kinetics compared to pure Cu. The higher electrochemically active surface area (ECSA) and the electrochemical double-layer capacitance ($C_{dl}$) values of CP/$CuO_x$ than those of CP/Cu and CP/$Cu_2O$ (Fig. 2c and ESI Fig. S11†) indicate more catalytically active sites on CP/$CuO_x$. Furthermore, EIS measurement was also used to further confirm the excellent electrocatalytic performance of CP/$CuO_x$. The Nyquist plots of EIS show that CP/$CuO_x$ exhibited a lower charge transfer impe-

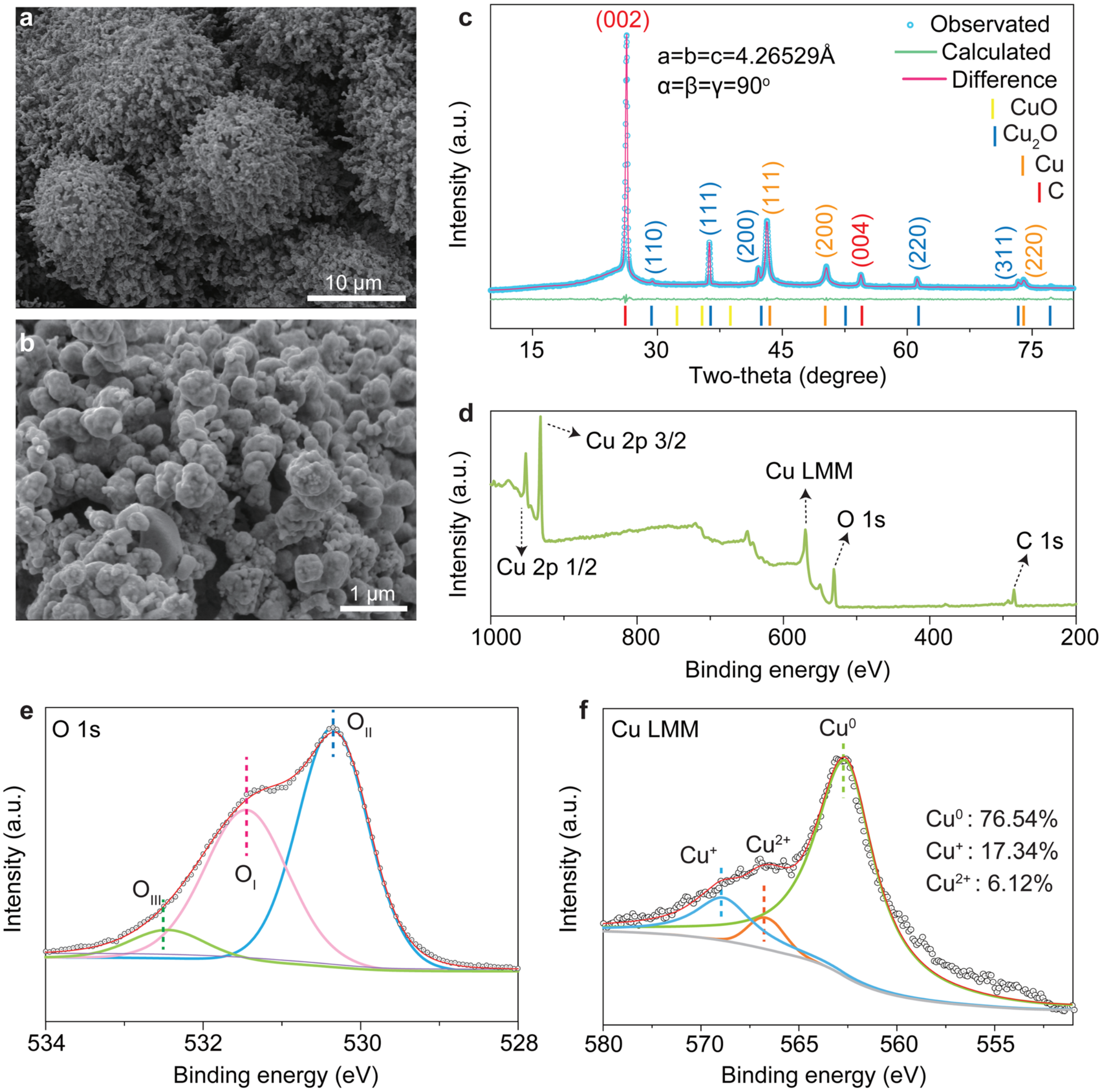

**Fig. 1** Characterization of CP/CuO$_x$. (a and b) SEM images of CP/CuO$_x$. (c) XRD patterns of CP/CuO$_x$ ($Cu_2O$: JCPDF No. 05-0667; CuO: JCPDF No. 48-1548; Cu: JCPDF No. 04-0836; C: JCPDF No. 23-0064). (d) XPS survey spectrum of CP/CuO$_x$. (e) High-resolution O 1s XPS spectrum and (f) high-resolution Cu LMM XPS spectrum of CP/CuO$_x$.

dance than the control groups, implying a more efficient electron transfer on the surface of CP/CuO$_x$ (Fig. 2d).

In the electrolysis experiments after 8 h, the CP/CuO$_x$ electrocatalyst was able to promote the conversion of $NO_3^-$ to $NH_4^+$ consistently and efficiently, with the intermediate product $NO_2^-$ almost not accumulating but being rapidly converted (Fig. 2e). In order to gain insight into the reduction of $NO_3^-$ to $NH_3$ over CP/CuO$_x$ in a mixed solution of 0.1 M $KNO_3$ and 1 M KOH, electrochemical *in situ* Raman spectroscopy measurements were performed at −0.6 V *vs.* RHE for a duration of 1 h. As shown in Fig. 2f, CP/CuO$_x$ shows peaks stretching at 730 and 1047 cm$^{-1}$, which were attributed to the vibrational modes of N–O ($NO_3^-$) and free $NO_3^-$ in the liquid environment.[41,42] The stretching intensity of these peaks increased gradually as the reaction time extended from 0 to 60 min, indicating the aggregation of $NO_3^-$ on the catalyst due probably to the strong adsorption of $NO_3^-$ on the CP/CuO$_x$ surface. The vibrational peaks at 1280 and 1548 cm$^{-1}$ are attributed to the reaction intermediates of $^*NO_2$ and *HON, and the Raman signals of these intermediates are weak during the reaction (ESI Fig. S12†).[43,44] Nevertheless, the Raman peak at 1664 cm$^{-1}$ attributed to $NH_2$ is clearly stronger.[45] These phenomena indicated that the $NO_3RR$ could rapidly convert to ammonia accompanied by some detectable intermediates through a stepwise deoxygenated hydrogenation pathway on the CP/CuO$_x$ cathode.

The efficient catalytic performance of CP/CuO$_x$ in ammonia production from nitrate reduction can be attributed to the suitable valence of Cu. With respect to the detailed role of Cu in each specific valence state, we tentatively considered them

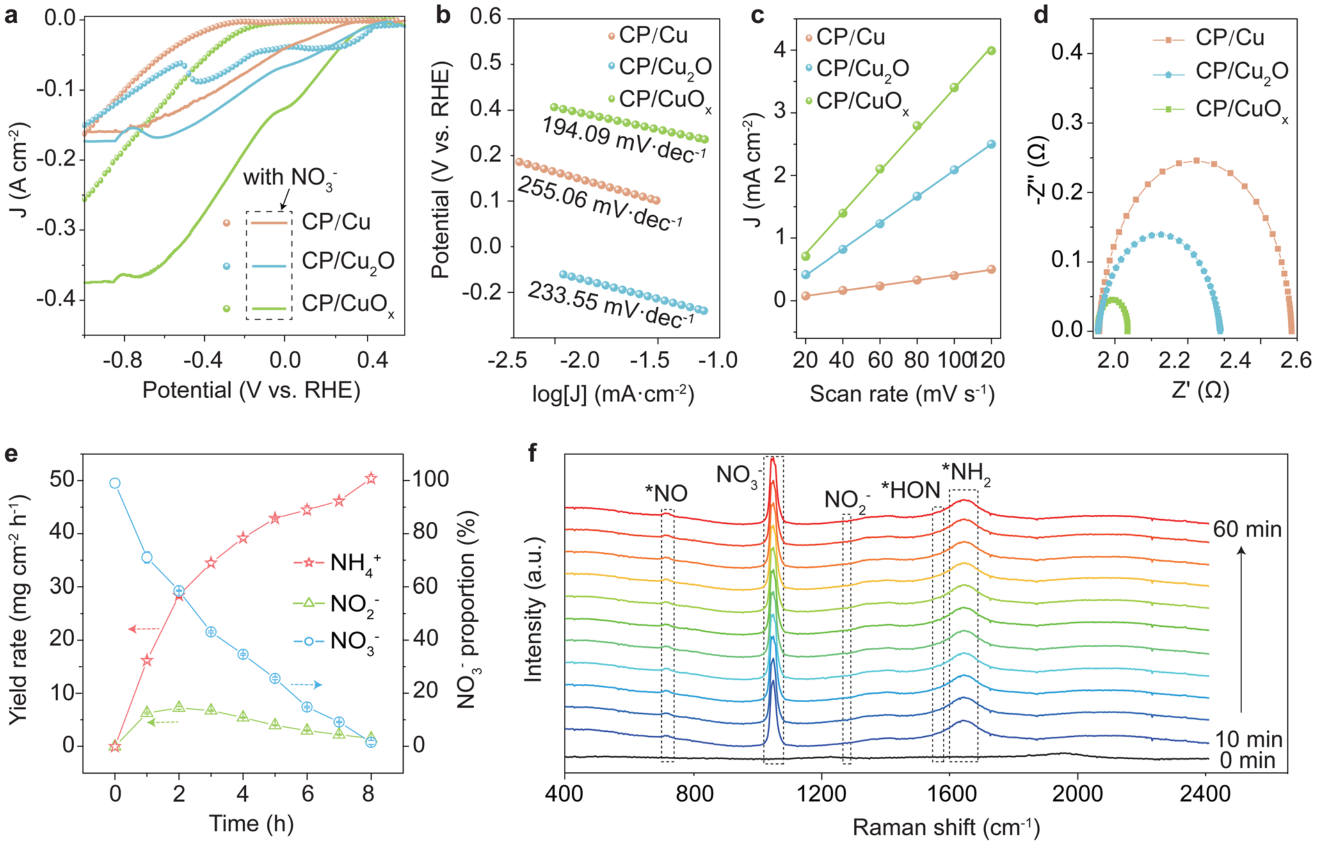

**Fig. 2** Electrochemical performance of CP/CuO$_x$. (a) LSV curve of CP/CuO$_x$. (b) Tafel slope of nitrate reduction by CP/CuO$_x$. (c) $C_{dl}$ of nitrate reduction for CP/CuO$_x$. (d) Nyquist plots of CP/CuO$_x$. (e) Eight hours of NO$_3$RR reaction process. 1 M KOH solution containing 0.1 M NO$_3^-$ as the electrolyte. (f) *In situ* Raman spectra of CP/CuO$_x$ during its electrochemical process.

from the viewpoint of Gibbs free energy of reaction intermediates (ESI Fig. S13†) by DFT calculations. The calculated results indicate that Cu$^0$ has a positive contribution to the conversion of NO$_3^-$ to *NH$_3$ but a thermodynamically unfavorable process is the desorption of *NH$_3$. Cu$^+$ displays a favorable NO$_3^-$ adsorption (*NO$_3$) compared to Cu$^0$ and Cu$^{2+}$ because of a higher downhill energy barrier of −4.02 eV, nevertheless only −1.88 and −1.84 eV on Cu$^0$ and Cu$^{2+}$ respectively. Unfortunately, Cu$^+$ has the very difficult step in the conversion of "*NO to *N" owing to an uphill energy barrier of 1.74 eV. Regarding Cu$^{2+}$, it almost displays all beneficial steps in coordinate numbers of 1–8 from the conversion of "NO$_3^-$ to *NH$_3$" aside from a slight uphill of 1.24 eV (*versus* 1.74 eV on Cu$^+$) in the foregoing step of "*NO to *N". Importantly, Cu$^{2+}$ displays the smallest uphill energy barrier for the final desorption of the *NH$_3$ intermediate which serves as the rate-determining step for Cu$^0$, Cu$^+$ and Cu$^{2+}$. Therefore, the valence composition of Cu plays a key role in our NO$_3$RR performance.

The performance of CP/CuO$_x$ in ammonia synthesis at different potentials (−0.1 to −1.0 V *vs.* RHE) was deeply investigated. To verify that ammonia production originated from the electrochemical reduction of NO$_3^-$ entirely, CP/CuO$_x$ was placed in electrolyte with and without NO$_3^-$ for electrocatalytic tests (please see 2.2 Ammonia electrosynthesis). As shown in ESI Fig. S14,† almost no ammonia generation was detected in the solution without NO$_3^-$, further confirming that the ammonia originated totally from the reduction of NO$_3^-$. The complementary $^{15}$N isotopic labeling experiment showed a typical double peak with chemical shifts at 6.85 and 6.97 ppm in the $^1$H NMR spectrum (ESI Fig. S15†), indicating the above similar conclusion. As shown in Fig. 3a and ESI Fig. S16a,† CP/CuO$_x$ exhibited faradaic efficiencies of more than 90% in the range of −0.3 to −1.0 V *vs.* RHE and realized a peak ammonia yield of 28.65 mg cm$^{-2}$ h$^{-1}$ at a potential of −0.9 V *vs.* RHE. Such high selectivity to NH$_3$ was probably attributed to the suitable adsorption energy and a favorable thermodynamic process for some key intermediates over our electrocatalyst. Other by-products such as H$_2$ or N$_2$H$_4$ were not detectable in our system (ESI Fig. S4, S5 and S17†). However, the faradaic efficiency still not being equal to 100% was probably attributed to the detectable reaction-incomplete intermediate NO$_2^-$ (Fig. 2e). CP/CuO$_x$ performed well in terms of ammonia yield and faradaic efficiency, well in agreement with the results of their LSV, ECSA, and EIS tests. A suitable potential of −0.6 V *vs.* RHE was chosen to test the long-term stability of CP/CuO$_x$, as can be seen in Fig. 3b. The results show that there was almost no performance attenuation in the continuous ammonia electrosynthesis with the CP/CuO$_x$ electrocatalyst

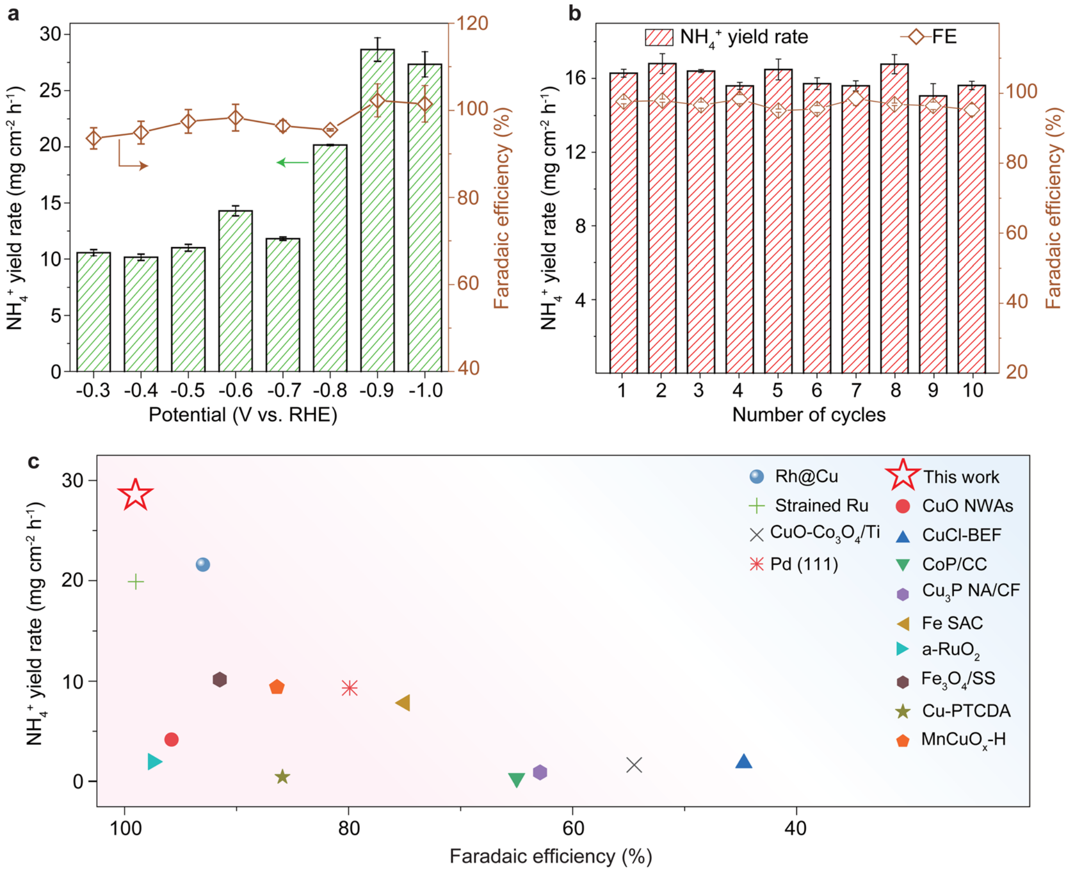

**Fig. 3** Ammonia electrosynthesis performance. (a) Faradaic efficiencies and $NH_4^+$ yields at different step potentials of CP/CuO$_x$. (b) The as-obtained faradaic efficiency and $NH_4^+$ yield during the cycling stability test of CP/CuO$_x$. (c) Performance comparison of ammonia electrosynthesis and its faradaic efficiency in the $NO_3RR$ between our work and the reported studies.

during 10 cycles. In addition, no significant changes were still observed in the CV curves (ESI Fig. S18†), Cu LMM XPS spectra (ESI Fig. S19a†) and Raman spectra (ESI Fig. S20†) of the catalysts before and after the reaction, and even the neglected Cu leaching (ESI Fig. S19b and c†) in each repeated run, together indicating that the catalyst composition remained robust even after ten cycle tests. Compared to the reported copper catalysts and other advanced catalysts, the CP/CuO$_x$ electrocatalyst in this study showed superior faradaic efficiency and $NH_4^+$ yield for the $NO_3RR$ (Fig. 3c and ESI Table S2†).

### 3.3 Unveiling of the role of conductivity in the reconstruction of CuO$_x$

To investigate the surface compositions and valence states of Cu for the $NO_3RR$, the CP/CuO$_x$, CP/CuO$_{x+1}$, CP/CuO$_{x+2}$ and CP/CuO$_{x+3}$ catalysts were prepared in 112, 128, 138 and 143 μS cm$^{-1}$ electrolyte, respectively, through an *in situ* electrochemical reconstruction process (please see 2.1 Working electrode preparation). Note that the increased oxygen element indicates the increased valence of copper. With increasing the conductivity of electrolyte from 128 to 143 μS cm$^{-1}$, the morphologies of CP/CuO$_{\&}$ ranged from a spherical-like cluster consisting of numerous rod-shaped copper grains (128 μS cm$^{-1}$, Fig. 4a) to irregularly distributed copper grains (138 μS cm$^{-1}$, Fig. 4b) and a more ordered distribution of large rod-like copper grains (143 μS cm$^{-1}$, Fig. 4c). Changes in the chemical compositions of these CP/CuO$_{\&}$ electrocatalysts were first detected by Raman spectroscopy (Fig. 4d). The characteristic Raman peaks of $Cu^+$ and $Cu^{2+}$ could be clearly observed, such as the stretching peak at about 300 cm$^{-1}$ pointed to the CuO ($Cu^{2+}$) phase.[46] This result is consistent with the valence changes revealed by XPS, as shown in Fig. 4e. In the XPS spectra of CP/CuO$_{x+1}$, CP/CuO$_{x+2}$ and CP/CuO$_{x+3}$, the signals of the $Cu^{2+}$ species become more prominent with increasing conductivity. The results indicate that the four catalysts consist of $Cu^0$, $Cu^+$ and $Cu^{2+}$ and that the amount of $Cu^{2+}$ increases from 6.94% to 25.91% with increasing conductivity (ESI Table S3†). In addition, the XRD results in ESI Fig. S21† support a similar conclusion, with the intensity of the Cu (100), (111) and Cu (220) facets decreasing progressively as the conductivity of electrolyte increases, while the intensities of the diffraction peaks representing the CuO phase increase gradually.

The *in situ* electrochemical reconstruction by CV was found to be two stages of dissolution (oxidation process) and redeposition (reduction process) of copper ions.[47] The $Cu^{2+}$ ions of the catalyst would leach into the electrolyte during the

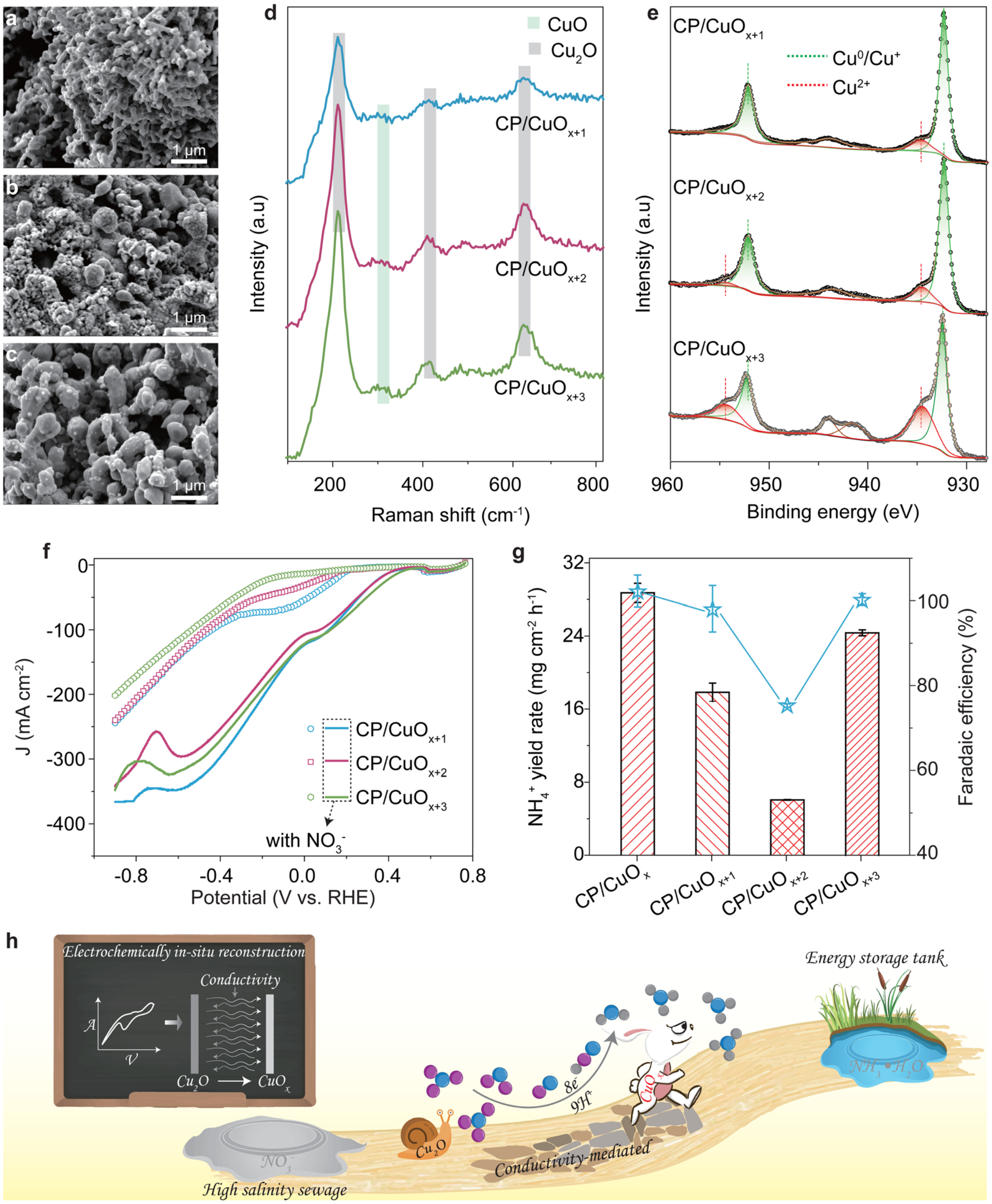

**Fig. 4** Conductivity-mediated electrochemical reconstruction of $CuO_\delta$. (a–c) SEM images of CP/$CuO_{x+1}$, CP/$CuO_{x+2}$ and CP/$CuO_{x+3}$. (d and e) Raman spectra and high-resolution Cu 2p XPS spectra of CP/$CuO_{x+1}$, CP/$CuO_{x+2}$ and CP/$CuO_{x+3}$. (f) LSV curves of CP/$CuO_{x+1}$, CP/$CuO_{x+2}$ and CP/$CuO_{x+3}$. (g) Faradaic efficiencies and $NH_4^+$ yields of CP/$CuO_{x+1}$, CP/$CuO_{x+2}$ and CP/$CuO_{x+3}$. (h) Schematic illustration of the conductivity-mediated *in situ* electrochemical reconstruction of $CuO_x$ for nitrate reduction to ammonia.

oxidation process, and then the $Cu^+$ or $Cu^0$ would redeposit onto the catalyst during the reduction process. A decrease in the conductivity of the electrolyte leads to an increase in electrical resistance, which slows down the ion migration rate in turn.[48] Consequently, in a low conductivity microenvironment, slow ion migration causes a higher accumulation of $Cu^{2+}$ on the catalyst surface. This would contribute to the formation of a clustered deposit with some lower valence copper during the reduction process (ESI Fig. S22†). In contrast, at higher conductivity, $Cu^{2+}$ ions can migrate and diffuse faster, resulting in a decrease in the local $Cu^{2+}$ concentration in the electrolyte which would cause the slight reduction of $Cu^{2+}$ on the catalyst ($Cu^{2+}{}_{liquid} \rightarrow Cu^0/Cu^+{}_{solid}$). Thus, we could obtain more $Cu^{2+}$ on the catalyst in a higher conductivity microenvironment (Fig. 4e and ESI Table S3†).

LSV analysis shows the current responses of CP/$CuO_{x+1}$, CP/$CuO_{x+2}$ and CP/$CuO_{x+3}$ to $NO_3^-$, and the current densities vary, in the sequence of CP/$CuO_{x+3}$ > CP/$CuO_{x+1}$ > CP/$CuO_{x+2}$

(Fig. 4f). This order is accordingly consistent with their ammonia yields and faradaic efficiency (Fig. 4g and ESI Fig. S16†). In terms of $NO_3RR$ performance, CP/$CuO_x$ produced with the lowest conductivity performs best, followed by CP/$CuO_{x+3}$ with the highest conductivity. The Raman spectrum of CP/$CuO_{x+3}$ was similar to that of CP/$CuO_x$ after 1 or 10 electrolysis experiments (ESI Fig. S20c†). The phenomenon indicates that CP/$CuO_{x+3}$ is unstable during electrolysis, and this would lead to a shift towards a similar chemical composition to CP/$CuO_x$, even for the initial CP/$CuO_{x+3}$ electrocatalyst with the highest $Cu^{2+}$ content. As a result, the $NO_3RR$ performance of CP/$CuO_{x+3}$ was close to that of CP/$CuO_x$ (Fig. 4g).

These results clearly indicate that conductivity-mediated *in situ* electrochemical reconstruction of $CuO_x$ can not only tune the physicochemical characteristics of catalysts, such as the physical morphology (Fig. 4a–c), but also, importantly, effectively control the valence state of copper which plays a key role in the $NO_3RR$ performance. The comparison of the $NO_3RR$ performance of CP/$CuO_x$ with that of CP/$Cu_2O$ and CP/Cu in Fig. 2a shows that the catalysts with all three valence states ($Cu^0$, $Cu^+$ and $Cu^{2+}$) exhibit desirable nitrate reduction. Furthermore, the results in Fig. 3 and 4f, g proved the significance of a suitable content of $Cu^{2+}$ in the $CuO_x$ electrocatalyst. The phenomena could be attributed to the easy formation of some key reaction intermediates during the $NO_3RR$ process and effective suppression of the competitive cathodic HER (see ESI Fig. S13 and S17†) on the $CuO_x$ interface.[49,50] Therefore, for achieving a high $NH_3$ yield during the $NO_3RR$ process, an appropriate conductivity microenvironment is needed to optimize the ratio of Cu valence states.

## 4. Conclusions

This study introduces a carbon fiber paper-supported $CuO_x$ nanoarray catalyst (CP/$CuO_x$) obtained by an *in situ* electrochemical reconstruction method for $NO_3^-$-to-$NH_3$ conversion. The CP/$CuO_x$ catalyst with various valence states of Cu shows an obvious improvement in $NO_3^-$-to-$NH_3$ conversion in comparison with CP/Cu and CP/$Cu_2O$. CP/$CuO_x$ with a suitable $Cu^{2+}$ content exhibited good stability, high faradaic efficiencies and high ammonia yields in a wide potential range. The results suggest that CP/$CuO_x$ obtained by the conductivity-mediated *in situ* electrochemical reconstruction route may provide a commercially competitive electrocatalyst for achieving excellent activity and selectivity of $NO_3^-$-to-$NH_3$ conversion (Fig. 4h).

## Author contributions

Hao Liang: methodology, data curation, formal analysis, and writing – original draft. Yinqiao Zhang: visualization and writing – review and editing. Xiaona Zhang: methodology and visualization. Erzhuo Zhao: validation and formal analysis. Wendan Xue: supervision and formal analysis. Enguang Nie: formal analysis and writing – review and editing. Minghua Zhou: writing – review and editing. Jianqiu Chen: methodology. Sijin Zuo: conceptualization, supervision, project administration, and funding acquisition.

## Conflicts of interest

There is no conflict of interest to declare.

## Acknowledgements

We are thankful for the financial support of the National Natural Science Foundation of China (No. 22306202 and 22306201) and the Natural Science Foundation of Jiangsu Province (No. BK20231026).

## References

1 K. Zhang, A. Cao, L. H. Wandall, J. Vernieres, J. Kibsgaard, J. K. Norskov and I. Chorkendorff, Spin-mediated promotion of Co catalysts for ammonia synthesis, *Science*, 2024, **383**, 1357–1363.

2 X. Zheng, J. C. Hao, Z. C. Zhuang, Q. Kang, X. F. Wang, S. L. Lu, F. Duan, M. L. Du and H. Zhu, Emerging electrospinning platform toward nanoparticle to single atom transformation for steering selectivity in ammonia synthesis, *Nanoscale*, 2024, **16**, 4047–4055.

3 S. T. Wang, Y. Liu, K. Zhang and S. Y. Gao, Self-powered electrocatalytic nitrate to ammonia driven by lightweight triboelectric nanogenerators for wind energy harvesting, *Nano Energy*, 2023, **112**, 108434.

4 S. Han, H. Li, T. Li, F. Chen, R. Yang, Y. Yu and B. Zhang, Ultralow overpotential nitrate reduction to ammonia via a three-step relay mechanism, *Nat. Catal.*, 2023, **6**, 402–414.

5 J. Chen, M. Q. Gu, Y. F. Zhou, D. J. Wan, Q. C. He, Y. H. Shi and Y. D. Liu, Efficient nitrate and perchlorate removal from aqueous solution via a novel electro-dialysis ion-exchange membrane bioreactor, *Chem. Eng. J.*, 2022, **430**, 132952.

6 J. Z. Qin, K. Wu, L. Z. Chen, X. T. Wang, Q. L. Zhao, B. J. Liu and Z. F. Ye, Achieving high selectivity for nitrate electrochemical reduction to ammonia over MOF-supported $Ru_xO_y$ clusters, *J. Mater. Chem. A*, 2022, **10**, 3963–3969.

7 L. Jia, H. Xue, F. Xian, Y. Sugahara, N. Sakai, J. Nan, Y. Yamauchi, T. Sasaki and R. Z. Ma, Porous and partially dehydrogenated $Fe^{2+}$-containing iron oxyhydroxide nanosheets for efficient electrochemical nitrogen reduction reaction (ENRR), *Small*, 2023, **19**, 2303221.

8 Z. C. Zheng, D. Wu, L. Chen, S. Chen, H. Wan, G. Chen, N. Zhang, X. Liu and R. Z. Ma, Collaborative optimization of thermodynamic and kinetic for Ni-based hydroxides in electrocatalytic urea oxidation reaction, *Appl. Catal., B*, 2024, **340**, 123214.

9 F. B. Yao, M. C. Jia, Q. Yang, F. Chen, Y. Zhong, S. J. Chen, L. He, Z. J. Pi, K. J. Hou, D. B. Wang and X. M. Li, Highly selective electrochemical nitrate reduction using copper phosphide self-supported copper foam electrode: Performance, mechanism, and application, *Water Res.*, 2021, **193**, 116881.

10 S. J. Zuo, W. D. Xue, Y. Q. Zhang, J. Q. Chen and Z. Q. Lin, Atomically dispersed Fe motif-based electrocatalysts for hydrogen peroxide synthesis, *ChemNanoMat*, 2024, **10**, e202300476.

11 B. Wang, X. Zhu, X. D. Pei, W. G. Liu, Y. C. Leng, X. W. Yu, C. Wang, L. H. Hu, Q. M. Su, C. P. Wu, Y. F. Yao, Z. Q. Lin and Z. G. Zou, Room-Temperature laser planting of high-loading single-atom catalysts for high-efficiency electrocatalytic hydrogen evolution, *J. Am. Chem. Soc.*, 2023, **145**, 13788–13795.

12 L. Fang, S. Wang, C. Song, X. H. Yang, Y. K. Li and H. Liu, Enhanced nitrate reduction reaction via efficient intermediate nitrite conversion on tunable $Cu_xNi_y$/NC electrocatalysts, *J. Hazard. Mater.*, 2022, **421**, 126628.

13 S. J. Zuo, R. X. Guo, W. D. Xue, J. G. Shang, J. Q. Chen and Y. Q. Zhang, Decipher the key role of ketone toward singlet oxygen evolution in Fenton-like process for water decontamination, *Appl. Catal., B*, 2023, **339**, 123100.

14 R. D. Zhao, Q. Y. Yan, L. H. Yu, T. Yan, X. Y. Zhu, Z. Y. Zhao, L. Liu and J. Y. Xi, A Bi–Co corridor construction effectively improving the selectivity of electrocatalytic nitrate reduction toward ammonia by nearly 100%, *Adv. Mater.*, 2023, **35**, 2306633.

15 J. Martínez, A. Ortiz and I. Ortiz, State-of-the-art and perspectives of the catalytic and electrocatalytic reduction of aqueous nitrates, *Appl. Catal., B*, 2017, **207**, 42–59.

16 J. N. Gao, B. Jiang, C. C. Ni, Y. F. Qi, Y. Q. Zhang, N. Oturan and M. A. Oturan, Non-precious $Co_3O_4$-$TiO_2$/Ti cathode based electrocatalytic nitrate reduction: Preparation, performance and mechanism, *Appl. Catal., B*, 2019, **254**, 391–402.

17 S. Liang, M. Y. Zhang, G. M. Biesold, W. Choi, Y. J. He, Z. L. Li, D. F. Shen and Z. Q. Lin, Recent advances in synthesis, properties, and applications of metal halide perovskite nanocrystals/polymer nanocomposites, *Adv. Mater.*, 2021, **33**, 2005888.

18 S. Xu, A. Dong, Y. Hu, Z. Yang, S. Huang and J. Qian, Multidimensional MOF-derived carbon nanomaterials for multifunctional applications, *J. Mater. Chem. A*, 2023, **11**, 9721–9747.

19 L. Liu, S. Zheng, H. Chen, J. Cai and S. Zang, Tandem nitrate-to-ammonia conversion on atomically precise silver nanocluster/MXene electrocatalyst, *Angew. Chem., Int. Ed.*, 2024, **63**, e202316910.

20 L. Cheng, Ti. Ma, B. Zhang, L. Huang, W. Guo, F. Hu, H. Zhu, Z. Wang, T. Zheng, D. Yang, C. Siu, Q. Liu, Y. Ren, C. Xia, B. Z. Tang and R. Ye, Steering the topological defects in amorphous laser-induced graphene for direct nitrate-to-ammonia electroreduction, *ACS Catal.*, 2022, **12**, 11639–11650.

21 R. Hao, Y. Song, L. Yang, Y. Guo, X. Wu, Z. Ma, Z. Qian, F. Liu, Z. Wu and L. Wang, Electrochemical reduction of flue gas denitrification wastewater to ammonia using a dual-defective $Cu_2O$@Cu heterojunction electrode, *Environ. Sci. Technol.*, 2024, **58**, 5557–5566.

22 E. Murphy, Y. Liu, I. Matanovic, M. Rüscher, Y. Huang, A. Ly, S. Guo, W. Zang, X. Yan, A. Martini, J. Timoshenko, B. R. Cuenya, I. V. Zenyuk, X. Pan, E. D. Spoerke and P. Atanassov, Elucidating electrochemical nitrate and nitrite reduction over atomically-dispersed transition metal sites, *Nat. Commun.*, 2023, **14**, 4554.

23 Z. Liu, F. Shen, L. Shi, Q. Tong, M. Tang, Y. Li, M. Peng, Z. Jiao, Y. Jiang, L. Ao, W. Fu, X. Lv, G. Jiang and L. Hou, Electronic structure optimization and proton-transfer enhancement on titanium oxide-supported copper nanoparticles for enhanced nitrogen recycling from nitrate-contaminated water, *Environ. Sci. Technol.*, 2023, **57**, 10117–10126.

24 Y. Li, J. X. Ma, Z. C. Wu and Z. W. Wang, Direct electron transfer coordinated by oxygen vacancies boosts selective nitrate reduction to $N_2$ on a Co-CuO electroactive filter, *Environ. Sci. Technol.*, 2022, **56**, 8673–8681.

25 A. Baghdasaryan and T. Bürgi, Copper nanoclusters: designed synthesis, structural diversity, and multiplatform applications, *Nanoscale*, 2021, **13**, 6283–6340.

26 H. Wu, L. Huang, J. Timoshenko, K. Qi, W. Wang, J. Liu, Y. Zhang, S. Yang, E. Petit, V. Flaud, J. Li, C. Salameh, P. Miele, L. Lajaunie, B. Cuenya, D. Rao and D. Voiry, Selective and energy-efficient electrosynthesis of ethylene from $CO_2$ by tuning the valence of Cu catalysts through aryl diazonium functionalization, *Nat. Energy*, 2024, **9**, 422–433.

27 Y. L. Zhao, Y. Liu, Z. J. Zhang, Z. K. Mo, C. Y. Wang and S. Y. Gao, Flower-like open-structured polycrystalline copper with synergistic multi-crystal plane for efficient electrocatalytic reduction of nitrate to ammonia, *Nano Energy*, 2022, **97**, 107124.

28 G. A. Cerrón-Calle, A. S. Fajardo, C. M. Sánchez-Sánchez and S. Garcia-Segura, Highly reactive Cu-Pt bimetallic 3D-electrocatalyst for selective nitrate reduction to ammonia, *Appl. Catal., B*, 2022, **302**, 120844.

29 Y. T. Wang, W. Zhou, R. R. Jia, Y. F. Yu and B. Zhang, Unveiling the activity origin of a copper-based electrocatalyst for selective nitrate reduction to ammonia, *Angew. Chem., Int. Ed.*, 2020, **59**, 5350–5354.

30 Y. H. Wang, A. Xu, Z. Y. Wang, L. S. Huang, J. Li, F. W. Li, J. Wicks, M. C. Luo, D. H. Nam, C. S. Tan, Y. Ding, J. W. Wu, Y. W. Lum, C. T. Dinh, D. Sinton, G. F. Zheng and E. H. Sargent, Enhanced nitrate-to-ammonia activity on copper-nickel alloys via tuning of intermediate adsorption, *J. Am. Chem. Soc.*, 2020, **142**, 5702–5708.

31 J. F. Su, I. Ruzybayev, I. Shah and C. P. Huang, The electrochemical reduction of nitrate over micro-architectured metal electrodes with stainless steel scaffold, *Appl. Catal., B*, 2016, **180**, 199–209.

32 Q. G. Zhu, X. F. Sun, D. X. Yang, J. Ma, X. C. Kang, L. R. Zheng, J. Zhang, Z. H. Wu and B. X. Han, Carbon

dioxide electroreduction to $C_2$ products over copper-cuprous oxide derived from electrosynthesized copper complex, *Nat. Commun.*, 2019, **10**, 3851.

33 R. L. Hao, Y. C. Song, L. L. Yang, Y. X. Guo, X. H. Wu, Z. Ma, Z. Qian, F. Liu and L. D. Wang, Electrochemical reduction of flue gas denitrification wastewater to ammonia using a dual-defective $Cu_2O$@Cu heterojunction electrode, *Environ. Sci. Technol.*, 2024, **58**, 5557–5566.

34 A. R. Puigdollers, P. Schlexer, S. Tosoni and G. Pacchioni, Increasing oxide reducibility: The role of metal/oxide interfaces in the formation of oxygen vacancies, *ACS Catal.*, 2017, **7**, 6493–6513.

35 F. Cavalca, R. Ferragut, S. Aghion, A. Eilert, O. Diaz-Morales, C. Liu, A. L. Koh, T. W. Hansen, L. G. M. Pettersson and A. Nilsson, Nature and distribution of stable subsurface oxygen in copper electrodes during electrochemical $CO_2$ reduction, *J. Phys. Chem. C*, 2017, **121**, 25003–25009.

36 J. Zhao, Z. Shen, J. Yu, Y. Guo, M. A. Mushtaq, Y. B. Ding, Z. Q. Song, W. Zhang, X. Huang, Y. Li, D. Q. Liu and X. K. Cai, Constructing Cu-CuO heterostructured skin on Cu cubes to promote electrocatalytic ammonia production from nitrate wastewater, *J. Hazard. Mater.*, 2022, **439**, 129653.

37 Z. J. Zhang, Y. Liu, X. Z. Su, Z. W. Zhao, Z. K. Mo, C. Y. Wang, Y. L. Zhao, Y. Chen and S. Y. Gao, Electro-triggered joule heating method to synthesize single-phase CuNi nano-alloy catalyst for efficient electrocatalytic nitrate reduction toward ammonia, *Nano Res.*, 2023, **10**, 6632–6641.

38 J. F. Zhang, Y. Wang, Z. Y. Li, S. Xia, R. Cai, L. Ma, T. Y. Zhang, O. Ackley, S. Z. Yang, Y. C. Wu and J. J. Wu, Grain boundary-derived $Cu^+/Cu^0$ interfaces in CuO nanosheets for low overpotential carbon dioxide electroreduction to ethylene, *Adv. Sci.*, 2022, **9**, 2200454.

39 S. Ingavale, P. Marbaniang, M. Palabathuni, V. N. Kale and N. Mishra, Decoration of boron nanoparticles on a graphene sheet for ammonia production from nitrate, *Nanoscale*, 2023, **15**, 11497–11505.

40 X. D. Wen and J. Q. Guan, Recent advancement in the electrocatalytic synthesis of ammonia, *Nanoscale*, 2020, **12**, 8065–8094.

41 Y. Liu, J. W. Ma, S. L. Huang, S. Y. Niu and S. Y. Gao, Highly dispersed copper-iron nanoalloy enhanced electrocatalytic reduction coupled with plasma oxidation for ammonia synthesis from ubiquitous air and water, *Nano Energy*, 2023, **117**, 108840.

42 X. Y. Li, P. Deng, M. Q. Xu, Z. B. Peng, Y. H. Zhou, G. Jia, W. Wang, P. Gao and W. Wang, Multi-layer core-shell metal oxide/nitride/carbon and its high-rate electroreduction of nitrate to ammonia, *Nanoscale*, 2023, **15**, 14439–14447.

43 Y. T. Wang, C. H. Wang, M. Y. Li, Y. F. Yu and B. Zhang, Nitrate electroreduction: Mechanism insight, *in situ* characterization, performance evaluation, and challenges, *Chem. Soc. Rev.*, 2021, **50**, 6720–6733.

44 F. C. Lei, K. Li, M. Yang, J. Yu, M. M. Xu, Y. M. Zhang, J. F. Xie, P. Hao, G. W. Cui and B. Tang, Electrochemical reduction of nitrate on silver surface and an *in situ* Raman spectroscopy study, *Inorg. Chem. Front.*, 2022, **9**, 2734–2740.

45 Y. H. Wang, S. S. Zheng, W. M. Yang, R. Y. Zhou, Q. F. He, P. Radjenovic, J. C. Dong, S. N. Li, J. X. Zheng, Z. L. Yang, G. Attard, F. Pan, Z. Q. Tian and J. F. Li, In situ Raman spectroscopy reveals the structure and dissociation of interfacial water, *Nature*, 2021, **600**, 81–85.

46 J. J. Zhou, F. Pan, Q. F. Yao, Y. Q. Zhu, H. R. Ma, J. F. Niu and J. P. Xie, Achieving efficient and stable electrochemical nitrate removal by *in situ* reconstruction of $Cu_2O$/Cu electroactive nanocatalysts on Cu foam, *Appl. Catal., B*, 2022, **317**, 121811.

47 G. C. Halford and M. L. Personick, Bridging colloidal and electrochemical nanoparticle growth with in situ electrochemical measurements, *Acc. Chem. Res.*, 2023, **56**, 1228–1238.

48 H. X. Sun and Z. F. Hu, Electrochemical behavior of Al-1.5Mg-0.05Sn-0.01Ga alloy in KOH ethanol-water solutions for Al-Air battery, *J. Electrochem. Soc.*, 2019, **166**, A2477–A2484.

49 Y. Xu, Y. S. Wen, T. L. Ren, H. J. Yu, K. Deng, Z. Q. Wang, X. N. Li, L. Wang and H. J. Wang, Engineering the surface chemical microenvironment over CuO nanowire arrays by polyaniline modification for efficient ammonia electrosynthesis from nitrate, *Appl. Catal., B*, 2023, **320**, 121981.

50 Y. Zhang, M. Q. Xu, X. D. Xu, X. Y. Li, G. P. Zhu, G. Jia, B. C. Yang, R. L. Yin, P. Gao and W. Ye, Efficient interlayer confined nitrate reduction reaction and oxygen generation enabled by interlayer expansion, *Nanoscale*, 2022, **15**, 204–214.